

Combining 2D and 3D Characterization Techniques for Determining Effects of HIP Rejuvenation After Fatigue Testing of SX Microstructures



A. DENNSTEDT, I. LOPEZ-GALILEA, B. RUTTERT, W. THEISEN, and M. BARTSCH

A hot isostatic pressing rejuvenation heat treatment is applied to a CMSX-4 type SX superalloy after it has been subjected to a low-cycle fatigue test to rupture. The evolution of microstructural defects, such as pores and cracks which are present after fatigue, has been tracked in 3D by X-ray tomography before and after rejuvenation. From the rejuvenated specimen, series of metallographic cross sections were prepared and investigated by scanning electron microscopy for getting complementary 2D information at high resolution. The micrographs were stitched to a panorama which was then matched into the 3D representation of the specimen volume. By combining 3D and 2D data, statistical volume-related quantities were achieved, while detailed characteristics have been assigned to individual defects present in the 2D panorama micrograph. This technique is in general appropriate for length-scale bridging microstructural investigations. Results of the performed investigations concerning the rejuvenation effect on the microstructure are presented and discussed.

<https://doi.org/10.1007/s11661-022-06914-9>
© The Author(s) 2022

I. INTRODUCTION

COMPONENTS for high temperature applications such as gas turbine blades are typically made of single-crystalline (SX) nickel base superalloys by casting.^[1,2] Cast parts exhibit microstructural inhomogeneities such as solidification pores and brittle intermetallic precipitates. If mechanical stresses are generated in service, either due to mechanical loads or a combination of thermal loads and mechanical constraints, pores and intermetallic precipitates such as topologically close-packed (TCP) phases act as stress concentrators, at which eventually cracks initiate. Once a crack is generated, it may propagate under creep or—more severely—under fatigue loads well below the materials yield strength and contributes to the failure of the component. Since the crack propagation rate depends on the length of the initial crack, which is related to the size of the related defect, processing technologies such as hot isostatic pressing (HIP) are

developed, resulting in smaller pore sizes. The effect of HIP has been evaluated for a wide range of load characteristics by Reference 3 showing a clear effect for the increase of fatigue life due to a reduction of porosity, while conventional HIP seems to have no significant effect on the creep life.

Innovative HIP facilities, which allow to integrate solid solution treatments and quenching or fast cooling in the HIP chamber, are now widely available and used by industry and research departments as well. Integrated HIP rejuvenation heat treatment has been carried out in the past successfully on specimens of CMSX-4 type material after interrupted creep tests, resulting in a high creep life time in repeated creep test due to the recovering of rafted γ - γ' microstructure and annihilating porosity.^[4-6] A positive effect of integrated HIP rejuvenation heat treatment on low-cycle fatigue (LCF) behavior has been shown for CMSX-4 material processed by casting or electron beam powder bed fusion (EPBF), respectively.^[7]

In this study, the microstructure of cast CMSX-4 material of a fatigue specimen has been characterized at first after the specimen fractured in LCF experiment and secondly after subsequent HIP rejuvenation heat treatment. 3D information achieved by X-ray tomography was correlated with details of individual defects investigated on metallographic sections, which were prepared after completing the 3D analyses. With this approach, the evolution of individual defects due to the HIP rejuvenation heat treatment has been captured.

A. DENNSTEDT and M. BARTSCH are with the Institute of Materials Research, German Aerospace Center, Linder Höhe, 51147 Cologne, Germany. Contact e-mail: Anne.Dennstedt@dlr.de I. LOPEZ-GALILEA, B. RUTTERT, and W. THEISEN are with the Materials Technology, Ruhr-Universität Bochum, Universitätsstr. 150, 44801 Bochum, Germany.

Manuscript submitted August 26, 2022; accepted November 16, 2022.

Article published online December 9, 2022

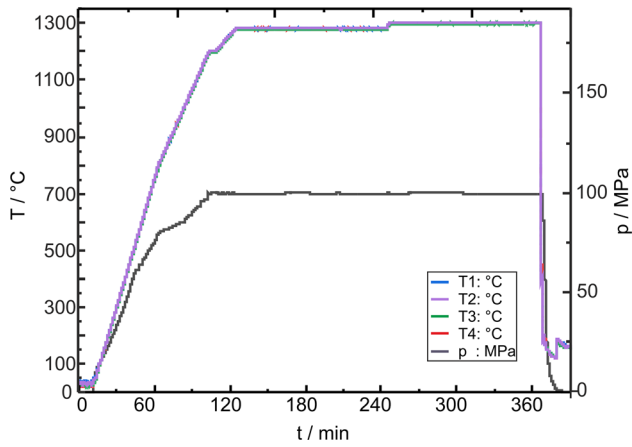


Fig. 1—Pressure and temperature applied during HIP rejuvenation treatment of sample B, which is prepared from one half of the fractured LCF specimen.

II. EXPERIMENTAL

A. Specimen and Samples

A Ni-base CMSX-4 type superalloy, denominated ERBO/1, was used in this study. The material was processed by casting and heat treated (solid solution and precipitation hardening). Detailed information on the material is documented in Reference 8. Investigations have been performed on a miniature fatigue specimen with a cylindrical measurement length of 6 mm and a corresponding diameter of 2 mm,^[9] which was manufactured with a [010] orientation parallel to the load axis. The LCF test was performed load-controlled at a temperature of 950 °C with a frequency of 0.25 Hz in tension–tension loading with a mean stress level of 550 MPa and a stress amplitude of 130 MPa and resulted in 2093 cycles to failure.^[10] The specimen has been elongated during the fatigue life cycle by cycle due to plastic deformation as a result of ratcheting associated to the positive mean stress. The plastic strain at failure was about 14 pct. Initial microscopic examination proved that numerous fatigue cracks emanated from internal casting pores.^[10] Both halves of the fractured specimen were investigated, with the bottom half in relation to the test configuration denominated ‘sample A’ and the upper part ‘sample B.’

B. Rejuvenation

The fatigued specimen underwent a rejuvenation procedure which was performed in the HIP with the goal to remove as much accumulated damage as possible such as rafting and porosity. HIP was carried out on sample B in a HIP system of type QIH-9 from Quintus Technologies AB equipped with a molybdenum furnace which was pressurized with argon. The HIP unit is able to operate at a maximum temperature of 1400 °C and a hydrostatic Ar pressure of maximum 207 MPa. A unique feature of the used HIP unit is that it allows to quench from high temperatures. The temperature is controlled by four Pt/PtRh thermocouples type B installed in the HIP furnace. The time and pressure

profiles during HIP exposure are shown in Figure 1. After a carefully selected heating rate, two extended temperature hold periods were applied at a constant pressure of 100 MPa, see Figure 1. At the end of the HIP process fast cooling was achieved by rapid Ar gas quenching. All details of the HIP rejuvenation procedure and the benefits on creep life have been described elsewhere.^[4–6] The HIP rejuvenation treatment has shown its beneficial impact on microstructures that suffered creep degradation (rafting, creep pores). It has been proved that it is possible to re-establish the original γ/γ' microstructure and simultaneously to close initial cast pores and creep pores. Consequently, the HIP rejuvenation resulted in an overall prolonged creep life.^[4–6] The fatigue specimen investigated here underwent HIP rejuvenation but no further thermal treatment.

C. Microstructural Investigations

The microstructure of the samples was evaluated by both two-dimensional and three-dimensional methods. Sample A was cut along the length axis, and a metallographic section was prepared and investigated by means of a scanning electron microscope (SEM), Zeiss Ultra 55, using an angular selective backscattered (AsB) electron detector.^[10] On sample B at first X-ray micro-computed tomography (μ -CT) was performed, in order to record the 3D representation of the microstructure after fracture in LCF but before HIP rejuvenation. Since μ -CT is a non-destructive, non-invasive characterization method of the internal structure of a specimen, sample B was afterward available and subsequently subjected to a HIP rejuvenation heat treatment. In order to track the changes that occurred due to this treatment, a second μ -CT tomogram was taken after completing the HIP rejuvenation.

For the μ -CT investigations, an EasyTom 160 unit from RX Solutions equipped with a nanofocus X-ray generator from Hamamatsu (LaB6 filament, max. 100 kV, 100 μ A) was used. Before starting the measurements, the sample was precisely oriented with the length axis of the sample gauge length aligned to the rotational axis of the CT sample holder. For image acquisition the acceleration voltage was set to 100 kV at a tube current of 55 μ A. In order to minimize artifacts, i.e., to correct the beam hardening from μ -CT scans, a Cu filter having a thickness of 0.4 mm was used. The radiographs were recorded by a flat panel detector with a pixel area of 1920×1536 pixels and a pixel size of 127 μ m, operating at a frame rate of 1.5 fps. During each measurement around 1340 projections were recorded. From the recorded X-ray projections, a 3D reconstruction of the inner structure of the sample was created *via* the filtered back projection method. Because of the selected scanning and reconstruction parameters, the voxel size was $1.4 \times 1.4 \times 1.4 \mu\text{m}^3$. The software AVIZO^[11] was applied for visualizing and analyzing the reconstructed data. A procedure consisting of ring artifact removal, beam hardening correction, and two three-dimensional filtering steps (median filter followed by delineate filter) was applied to each reconstructed volume. After

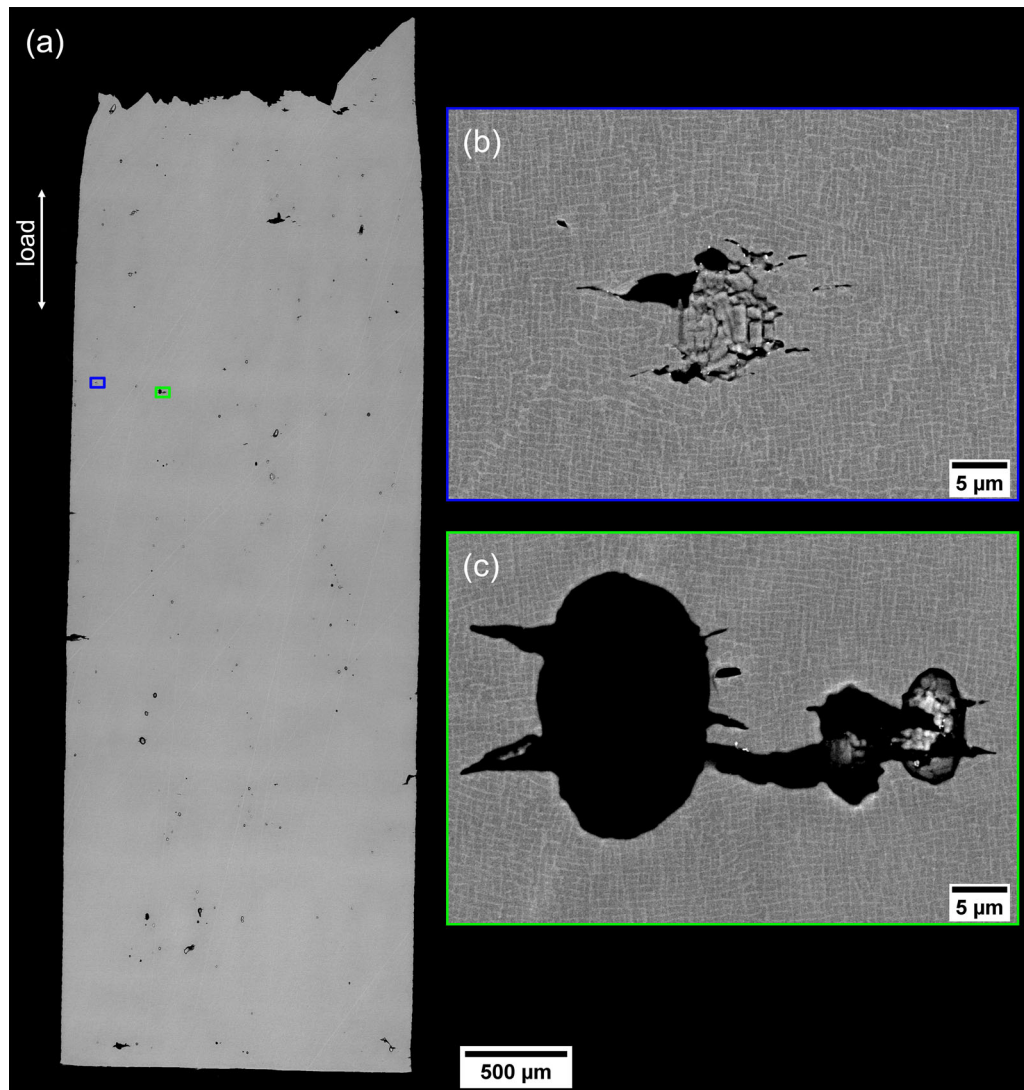


Fig. 2—Longitudinal section of the sample A, prepared from one half of the fractured LCF specimen, observed in BSE mode with AsB detector (a), detail of one pore showing the locally deformed $\gamma-\gamma'$ microstructure (b), and detail of a defect consisting of two solidification pores with cracks emanating from the pores (c) (Color figure online).

performing the alignment of the corresponding volumes of the sample before and after rejuvenation (details are given in the next section of this paper), a detailed segmentation was performed using the watershed segmentation tool of AVIZO. Ambient occlusion^[12] was applied in order to differentiate air filled pores and open cracks from the surrounding air. Segmentation of the ambient occlusion field was performed using the Magic Wand tool and the Threshold tool of AVIZO's segmentation editor resulting in the differentiation of internal pores and cracks from defects at the surface.

Finally, series of metallographic length sections were produced from sample B by subsequently grinding parallel layers starting from the circumference. From each prepared section, overlapping high-resolution micrographs were taken using a field-emission SEM type LEO 1530 VP. Automatized stage scans (surface map) were applied in both the secondary electron contrast mode (SE) and the backscattered contrast

mode (BSE). At a working distance of 8.5 mm and with a magnification of 500 x, several individual micrographs were taken with a 10 pct overlay to capture the entire length section. The individual micrographs were subsequently stitched together to one large-scale high-resolution montage.

III. COMBINATION OF MICROSTRUCTURAL DATA

In this study, different methods were used to investigate the microstructure evolution at different stages of the process in separate experiments. In order to know which microstructural changes developed due to the HIP rejuvenation treatment, an alignment of the different datasets was performed. Three types of variations occur in the datasets all together^[13]: variations due to the differences in acquisition can cause misaligned

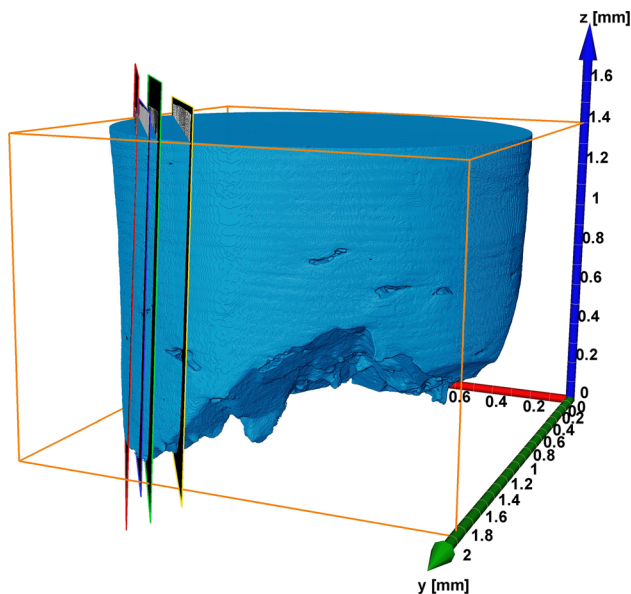


Fig. 3—3D representation of sample B from the fractured LCF specimen, using a perspective camera. In addition to the specimen surface (shown in blue) the positions of the metallographic sections prepared after the HIP rejuvenation treatment are shown with differently colored frames: red corresponds to Fig. 9(a), blue to Fig. 9(c), and green to Fig. 9(e) and Fig. 8. The yellow framed section indicates a plane cutting a larger crack at the sample surface which has been used for matching 2D and 3D datasets (Color figure online).

images (1) and/or, more severe, differences in lighting (2). Also differences between the images (3) caused by changes of the observed objects have to be considered. For the task of finding a transformation that the points in one dataset can be related to the points in the other, which is called registration, different classes of registration problems appear. For example, datasets originating from different sensors (μ -CT and SEM) should be combined as well as datasets showing different states of the specimen. The 2D image (SEM) can be considered as a template that is attempted to be located in the 3D volume. The registration methods can be divided into feature-based and intensity-based techniques.^[14]

Three different types of alignment were applied in this study because the microstructural data belong to different dimensions:

- (1) A 3D–3D alignment: align the CT volumes of the sample before and after HIP rejuvenation to detect the changes inside the volume,
- (2) A 2D–2D alignment: align the single SEM images collected systematically on different longitudinal sections to obtain a stitched overview on the sections, and
- (3) A 2D–3D alignment: the alignment of the SEM images (2D) to the CT volume (3D) to identify and examine interesting individual features by means of the SEM images with high resolution.

The first alignment to get the same orientation for both CT volumes before and after HIP treatment was performed in AVIZO using different features at the specimen surface obtained after a first threshold

segmentation. After defining the feature positions in both volumes by using the landmarks-2-sets-object of AVIZO, the transformation matrix was calculated and applied resulting in two equally orientated volumes.

The second alignment was performed for the image stack collected in the SEM using software Image Composite Editor (ICE).^[15]

The third alignment was finding the position of the SEM image inside the CT volume. This was done manually using the software AVIZO. After preparing and capturing several large-scale montages the defects at the specimen surface could be used as landmarks to identify the position of the sections, especially the large cracks are very helpful to succeed this task. After finding the position of the first section the other ones were looked for in parallel slices to the first one.

IV. RESULTS

A. Microstructural Defects After Rupture in LCF

Sample A has experienced the LCF experiment until rupture but not the HIP rejuvenation heat treatment. Figure 2 shows SEM micrographs of the longitudinal section of sample A, an overview in Figure 2(a) and details of pores with cracks emanating from these pores in Figures 2(b) and (c).^[16] The pores are large solidification pores having diameter values up to $50\ \mu\text{m}$, and many of them show clearly the evolution of cracks. As formerly reported,^[10] the pores in this material have average sizes of about $10\ \mu\text{m}$. On fracture surfaces the pores appear as almost circular structures which are typically located in the center of square-shaped facets with edge lengths of 10 to $30\ \mu\text{m}$, as shown in References 7 and 10. These facets indicate the crack path of slow crack growth in the LCF experiments.

Figure 3 displays the three-dimensional shape of sample B, which was used for μ -CT investigations in this study. The flat surface on top was produced during preparation after the LCF experiment, whereas the lower, rough surface is caused by the rupture. Pores and pores with emanating LCF cracks, respectively, are shown in the visualization of the 3D volume in Figures 4(a) and (c). The different coloring of the defects was done to indicate if they have contact to the surface (red) or if they are enclosed and isolated from the sample surface (internal defects, yellow). Figure 4(a) is a view from the side and represents a view parallel to the growth direction of the dendrites inside the specimen. The majority of pores are located in spaces between the dendrites, and thus the dendrites themselves become visible due to nearly blank (pore-free) areas. Figure 4(c) shows a top view, parallel to the load axis in LCF, along a [010] direction. In this view, the linear arrangement of pores within the interdendritic space becomes visible.

Histograms showing the size distribution of internal defects and such connected to the surface both before and after HIP rejuvenation are displayed in Figure 5. The selected class width was $3.4\text{E}-04\ \text{mm}^3$. Small defects with volumes of less than $5\text{E}-04\ \text{mm}^3$ show

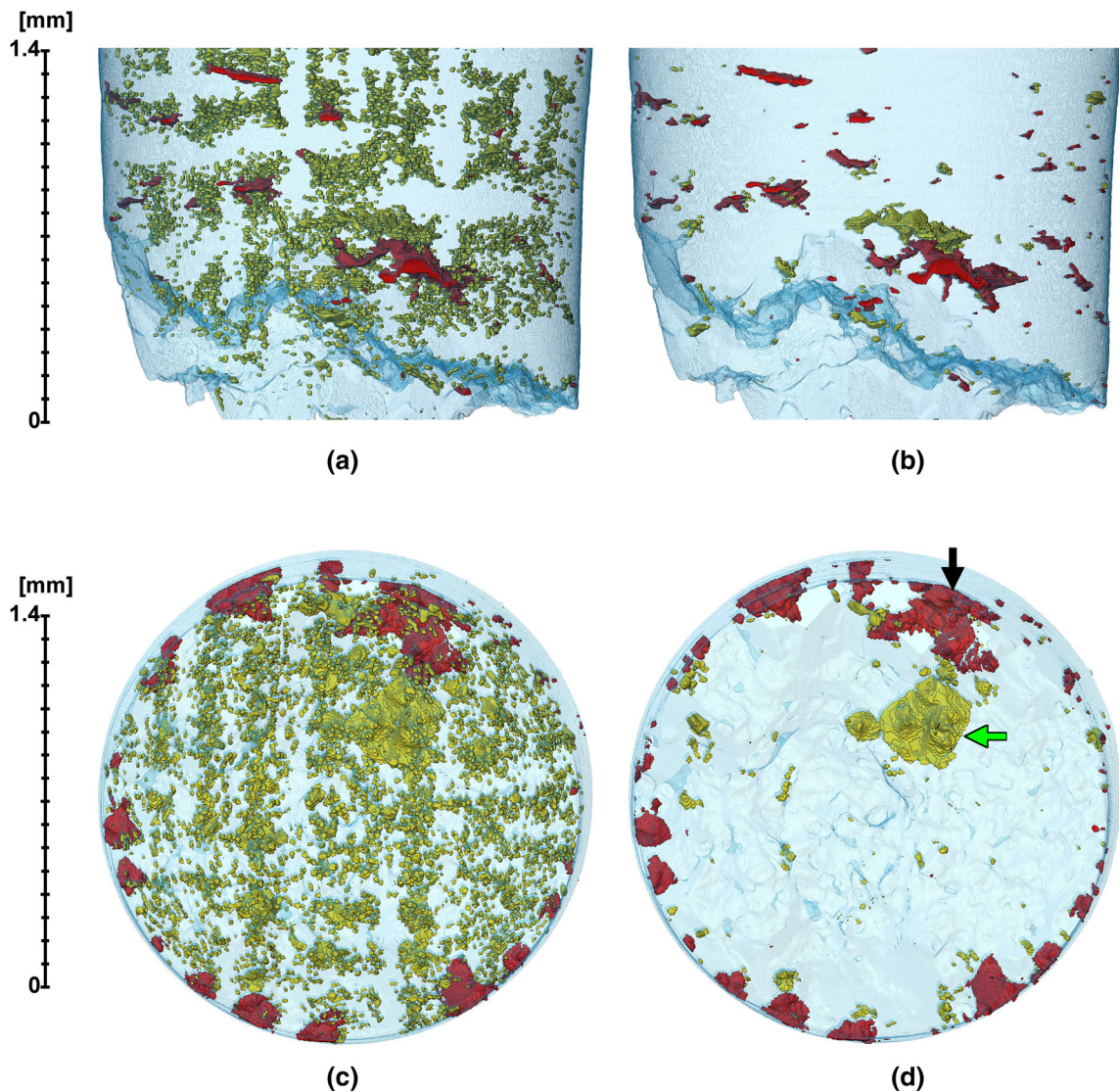


Fig. 4—3D representation of CT volume of sample B from the fractured LCF specimen before (left) and after (right) HIP rejuvenation treatment, using an orthographic camera. The material containing defects is not shown, and the sample surface is shown as light blue transparent contour. Inside the bluish contour defects at the surface or connected to the surface are shown in red and the internal defects in yellow, (a) and (b) sideview, (c) and (d) view parallel to load direction. The arrows in (d) indicate the two largest defects (Color figure online).

the highest rate in all cases. The majority of small internal defects (left histograms) displayed volumes smaller than $5\text{E}-04\text{ mm}^3$. However, one large defect with a volume of about $3.4\text{E}-03\text{ mm}^3$ was counted and can be associated to the largest apparently internal defect (colored in yellow and highlighted by the green arrow in Figure 4(d)). In this viewing direction, this defect has a diameter of about $600\text{ }\mu\text{m}$.

B. Microstructural Defects After HIP Rejuvenation

In general, a HIP rejuvenation heat treatment is applied in order to re-establish an as-new condition on a microstructural level, where γ' precipitates after solution at high temperature are re-precipitated and all pores are annihilated. The effect of the HIP rejuvenation process used in this study gets visible by comparing left and right images of Figure 4, where the three-dimensional spatial

distributions of the defects in sample B are illustrated before and after the HIP process. A reduction in number and size of pores and cracks is observed, and it seems that only large defects remain. Comparing the histograms before and after HIP rejuvenation displayed in Figure 5, it is obvious that the number of small internal defects (left histograms) was reduced due to the HIP rejuvenation by about one order of magnitude. However, the one large defect having a volume of about $3.4\text{E}-03\text{ mm}^3$ before HIP rejuvenation is still there, but its size seems decreased to about $3.3\text{E}-03\text{ mm}^3$. In contrast, the number and size of defects in contact with the surface (right histograms) did not considerably change due to HIP rejuvenation, except one individual large defect having a volume of about $2.4\text{E}-03\text{ mm}^3$ before and $2.1\text{E}-03\text{ mm}^3$ after HIP rejuvenation. This defect colored in red is marked with a black arrow in Figure 4(d) and is situated next to the largest, apparently

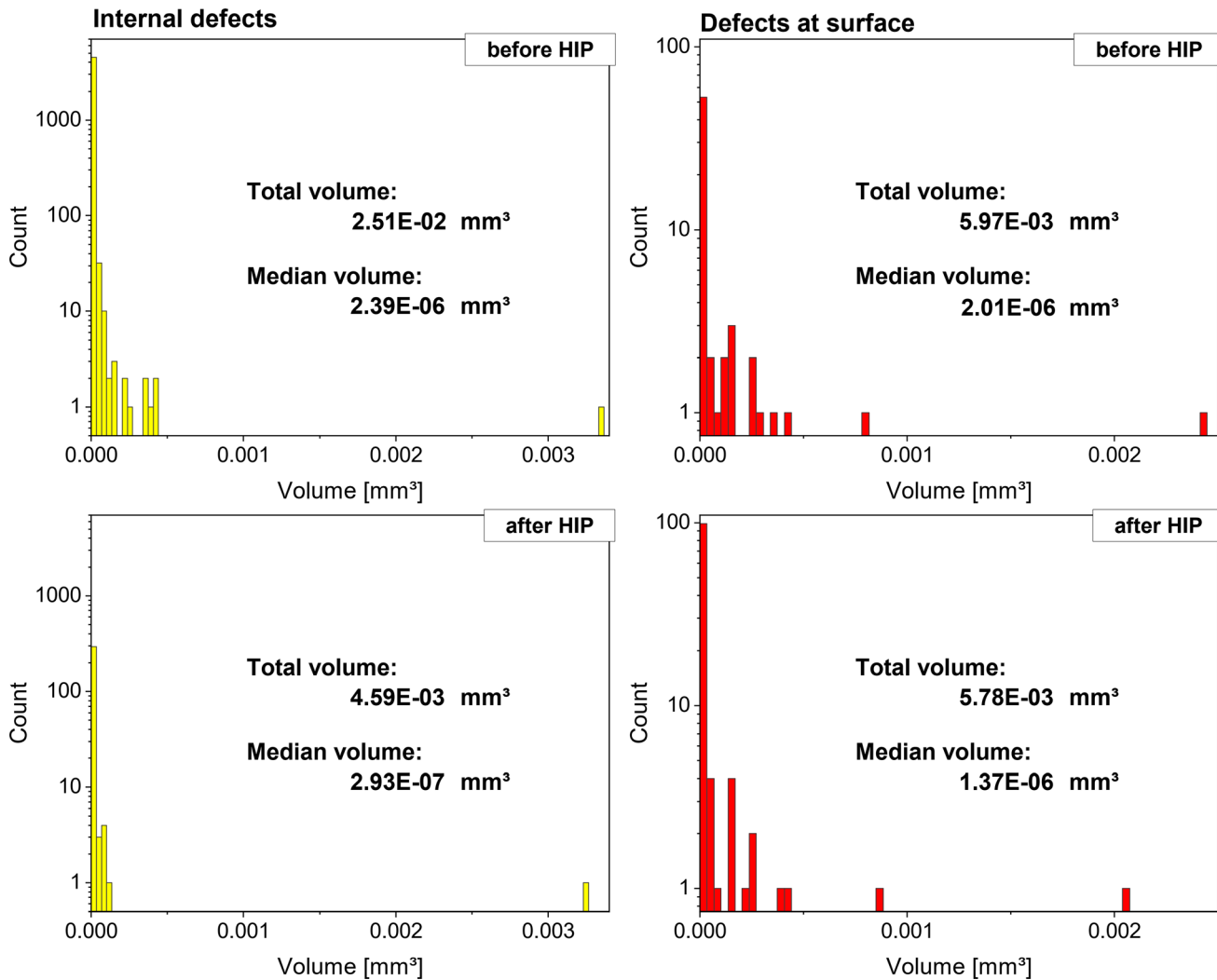


Fig. 5—Histograms showing the frequency of counted defects differentiated in internal defects and such at surface, before and after HIP rejuvenation treatment. Colors correspond to the color code in Fig. 4 (Color figure online).

internal, defect colored in yellow and marked with the green arrow.

In addition to counting the defects with their different volumes, it is possible to consider the virtual 3D representation of a sample as a stack of images and to analyze single slices. Such slices perpendicular to the load axis in LCF are shown in Figure 6. The bright areas represent the sample, whereas the dark areas represent the defects and the surrounding. Slices on the left side (Figures 6(a), (c), and (e)) show the situation before and the slices on the right side (Figures 6(b), (d), and (f)) show the situation after HIP rejuvenation.

In Figure 7, the results of the quantitative analysis of the defect area fractions in all evaluated virtual slices are plotted. The thinner blue lines represent the results after LCF, before the HIP rejuvenation process was applied and the thicker black lines represent the results after the HIP rejuvenation process. The results are plotted against the “distance to fracture surface,” where the fracture surface is defined as the bottom line in the volume representations of Figures 4(a) and (b). The area

of the specimen in each slice is composed of the sample, the internal defects, and the defects at the surface. This area is shown as dotted line in Figure 7(a) and shows an increase with increasing distance to the fracture surface because of the necking of the LCF specimen at the fracture site, shortly before failure. Additional lines in this plot represent the defect fraction in each slice, which is the ratio of areas of defects (internal and at the surface together) to the entire area of the specimen. The fraction varies between the different slices, with slices displaying high defect fractions located in interdendritic planes, while slices with low defect fractions comprise more dendrite material (compare Figure 4). Over all, after the HIP rejuvenation process, the defect fraction is reduced. The plot in Figure 7(b) shows the area that is assigned to the defects connected to the surface that are shown in Figure 4 in red. There are slices with larger (red) areas that coincide with surface cracks. The size of these areas does not change considerably after the HIP rejuvenation process. In contrast, the plot in Figure 7(c) shows the areas of the internal defects that are shown in Figure 4

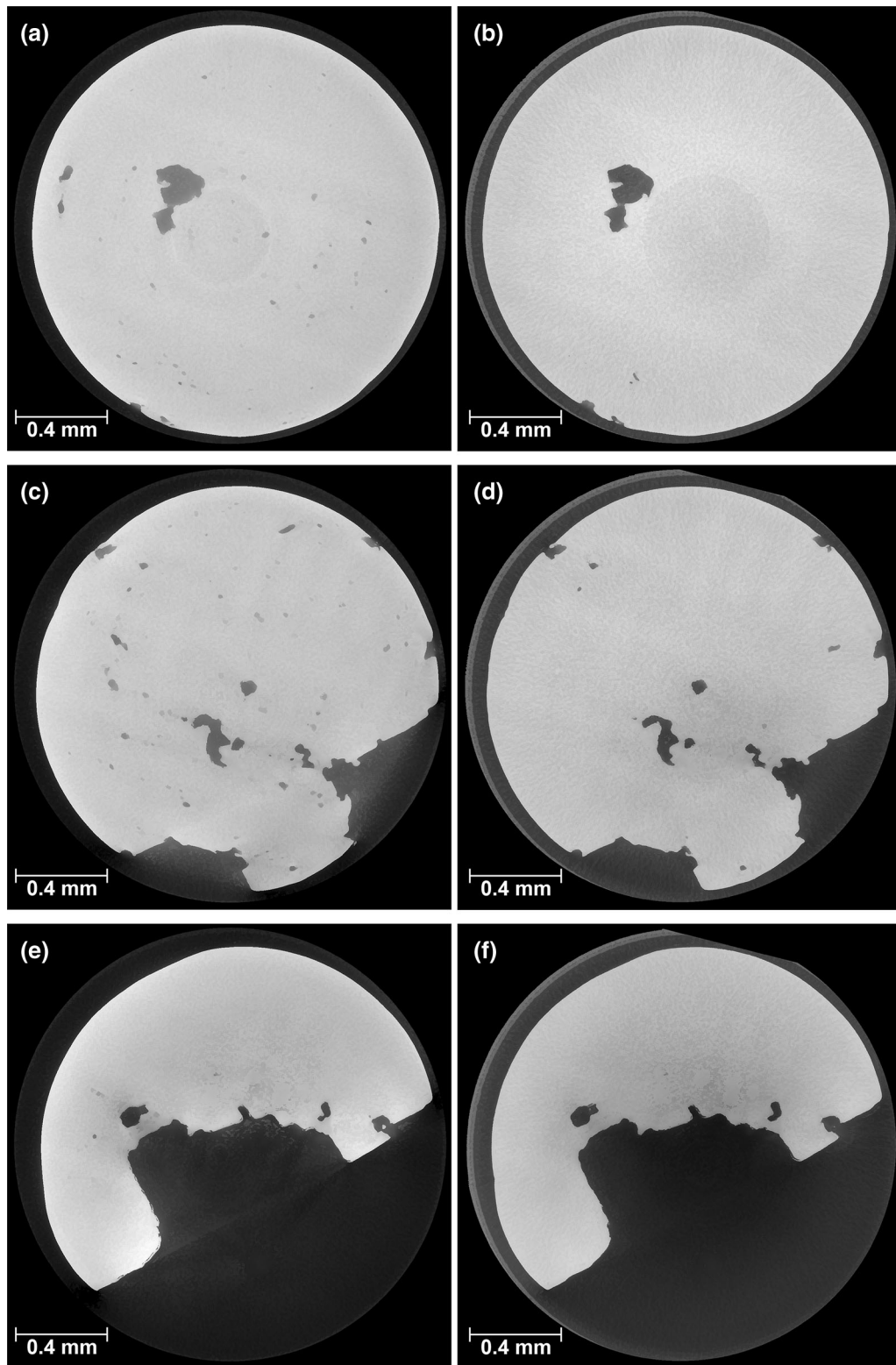


Fig. 6—Slices from CT volume of sample B from the fractured LCF specimen before (left) and after HIP rejuvenation (right). The slices are oriented normal to the load direction showing the situation at a distance from fracture surface of 0.75 mm ((a) and (b)), 0.5 mm ((c) and (d)), and 0.25 mm ((e) and (f)). Bright area is the alloy, whereas the dark areas represent defects and the surrounding air.

in yellow. In general, the defect areas in this plot are decreased after the HIP rejuvenation process showing the closure of defects isolated from the surface.

Thus, the common inspection of Figures 6 and 7 discloses three different scenarios mainly based on the different defect areas of the internal defects. Figures 6(a)

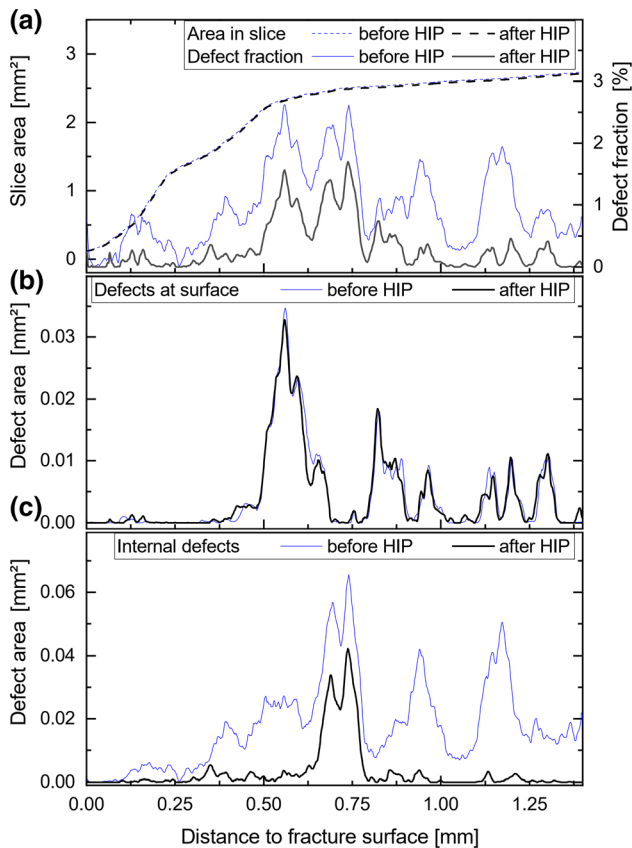


Fig. 7—Evolution of defect fraction in virtual slices of the 3D volume due to the HIP rejuvenation procedure for slices normal to the load direction. Plotted for each slice with increasing distance to the fracture surface are: (a) area of sample and defect fraction, (b) area of defects at the surface, and (c) area of internal defects.

and (b) show the slice pair at a distance of about 0.75 mm to the fracture surface, and for this position a decrease of the area of the internal defects can be seen in Figure 7(c). However, a large area of internal defects is still remaining after the HIP rejuvenation process. This area is mainly caused by the large pore in Figures 6(a) and (b), and which is also part of the large yellow pore shown in Figures 4(b) and (d). The image pair in Figures 6(c) and (d) represents a slice at a distance of about 0.5 mm to the fracture surface, and the decrease of the area of internal defects in Figure 7(c) results nearly in zero. Almost all internal defects disappeared due to HIP rejuvenation, while larger defects that are still visible in Figure 6(d) are defects at the surface, and Figure 7(b) shows for this position a remarkable area of defects at the surface. The slice pair in Figures 6(e) and (f) is located about 0.25 mm from fracture surface which is a region with a low defect fraction (Figure 7(a)), and the area of internal defects in Figure 7(c) reduces from a low value to nearly zero.

After the second CT imaging, sample B was embedded, and longitudinal sections were prepared metallographically and observed with SEM. In order to obtain an overview, adjoined images were collected and

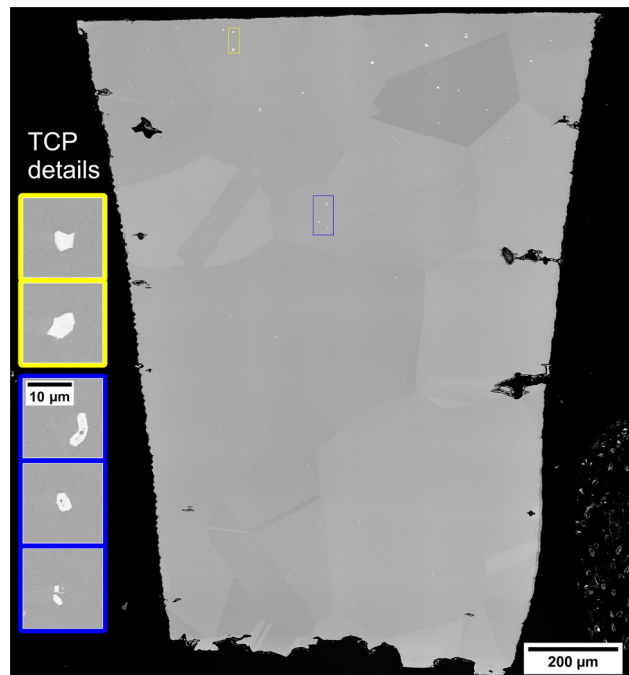


Fig. 8—SEM micrograph of a metallographic section of sample B after HIP rejuvenation, composed of stitched images of high resolution, captured in BSE mode. The different gray levels show the polycrystalline nature of the sample. Insets on the left show $\times 10$ magnified details of several TCP particles—both near to the edge of the section as well as in the center of the section, as indicated by the two frames on the section.

afterward stitched together. One of these overviews is shown in Figure 8 as well as depicted as the layer with the green frame in Figure 3. The different gray levels make clearly visible that there are now different crystal orientations in the specimens, which means that the single crystalline material totally recrystallized.

The lower border of the sample in these images is the fracture surface, while the top border was produced by sample preparation after the LCF experiment. At the fracture surface are many kinks visible. Longer straight lines at this lower border occur when facets are cut that have been developed during LCF crack growth before fracture. The lateral borders reflect the surface of the specimens and show in black several cracks that were treated as surface defects in the 3D analysis. Only few large defects are visible in this length section which seem to be isolated from the surface.

A quantification of the internal defects, i.e., of those defects without a clear connection to the surface, is carried out in the 2D cross section shown in Figure 8 (SEM), as well as in the corresponding section recorded by the μ -CT investigations, and represented in Figure 3 with a green frame. A value of 0.19 area pct was obtained from the quantification of the images recorded at the SEM, while 0.17 area pct was quantified in the slice extracted from the 3D CT volume. The higher value measured by SEM characterization may be related to the higher resolution of the SEM quantification technique with respect to μ -CT. The detailed quantification carried out in the 2D SEM cross section allows

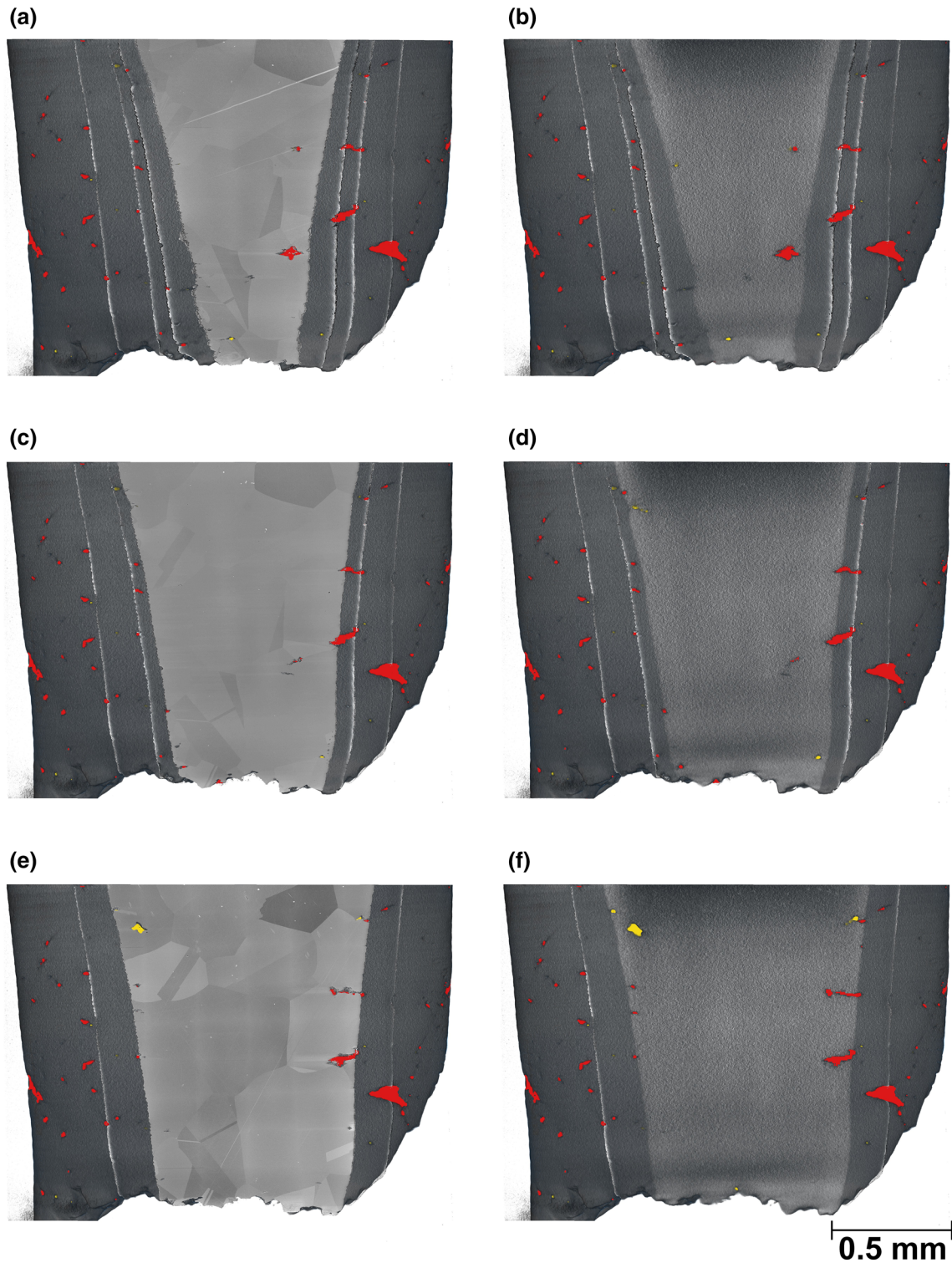


Fig. 9—Comparison of virtual sections of the CT volume with stitched SEM images matching to the CT volume, left images: SEM image is shown on top of the section of CT volume, right images: solely the section of the CT volume is shown. Bright lines right and left of the sections indicate the consecutive sections. The sections correspond to layers indicated in Fig. 3: red framed layer in (a) and (b), blue framed layer in (c) and (d), and green framed layer in (e) and (f). For this representation an orthographic camera is used (Color figure online).

the identification of defects that, although they do not have a visual connection with the surface, present an oxidation layer in their interior volume. Of the total

internal defects quantified in 2D (0.19 area pct), the pores that do not have the presence of an oxidation layer represent 0.12 pct of the area.

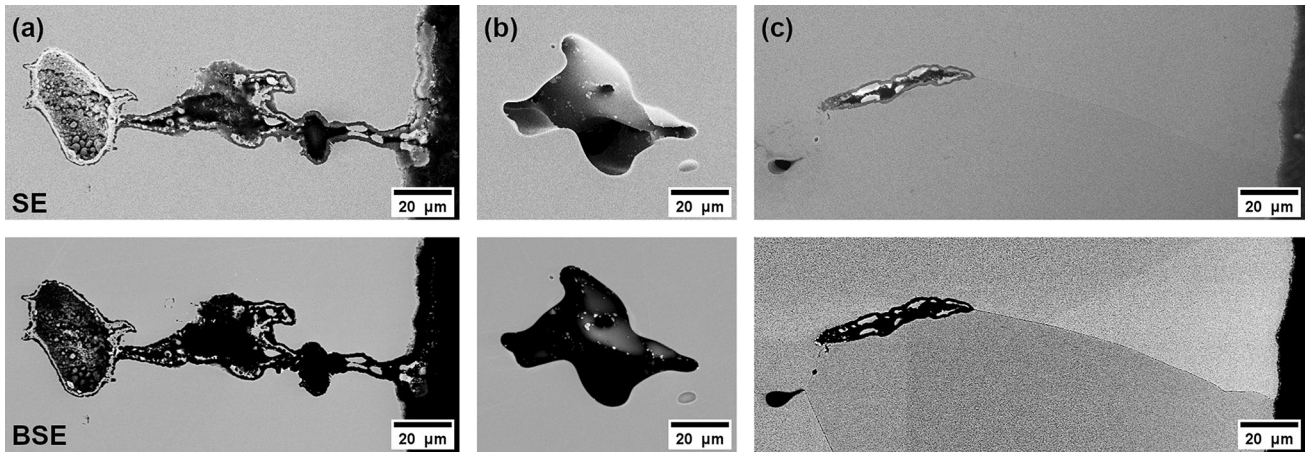


Fig. 10—SEM images of different pores, both in SE (top) and BSE mode (bottom). In (a) a pore with cracks connected to the surface that was assigned as defect at surface, in (b) an internal pore, and in (c) an apparently internal pore, but with inner oxide layer indicating a connection to the surface.

In addition to pores and cracks, tiny white areas representing intermetallic precipitates are also observed in recorded images in 2D (Figure 8) and 3D. The white intermetallic phases are presumably TCP phases, some of them are magnified shown as insets in Figure 8.

C. Combination of CT and SEM Characterization Techniques

The result of the registration process, i.e., the combination of microstructural data as described in section III, is shown in Figure 9, where three combinations of CT volumes with images of metallographic sections are matched. On the left side of the figure (Figures 9(a), (c), and (e)), the SEM montage is positioned on the virtual cut of the CT volume, whereas on the right side (Figures 9(b), (d), and (f)) the cut volume is shown without this overlayer. The defects are shown in yellow and red assigned to internal defects or such connected with the surface, consistent to the color code applied in Figures 4 and 5.

This registration result is used to check interesting pores as exemplified in Figure 10. In Figure 10(a), a pore is shown that was detected as defect at the surface, and it shows clearly an oxide layer on the inner surface. In Figure 10(b), an example of internal pores is shown—no oxide layer is detectable on the inner surface of this pore. In Figure 10(c), a defect which was assigned initially as internal defect is displayed that clearly shows an oxide layer on the inner surface. Thus, it can be concluded that this defect has small/tiny cracks connected to the surface, which were not detected by CT but allow for gas transport to the internal.

V. DISCUSSION

A. Challenges in Combining Microstructural Characterization in 2D (SEM) and 3D (CT)

The aim of this study was to combine 3D data obtained from CT with 2D data obtained from SEM in order to get a better understanding on how a

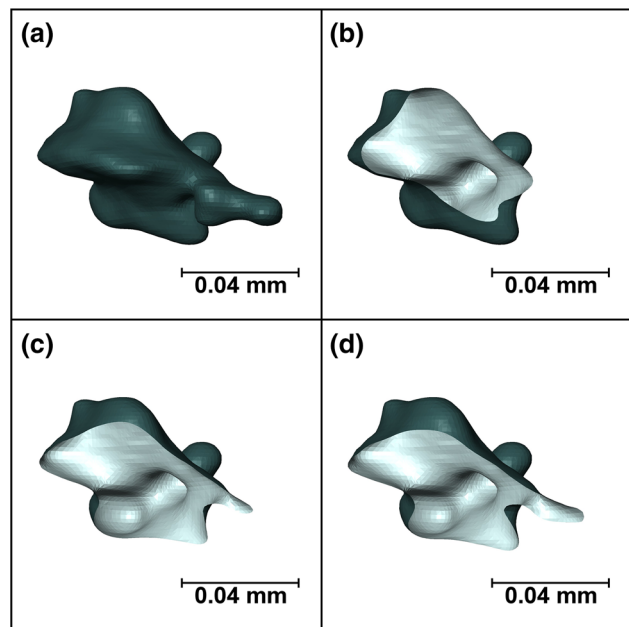


Fig. 11—The three-dimensional representation of the pore shown in Fig. 10(b), using an orthographic camera. (a) Showing the surface of the pore, (b) showing the section by the orientated layer indicated with a green frame in Fig. 3, (c) showing the section with a slightly tilted layer compared to (b), and (d) showing a section with a layer moved slightly parallel with respect to the layer in (c). The bright area is the visible internal surface (Color figure online).

rejuvenation treatment can be applied on microstructures which were subjected to LCF loading. Registration is the process to bring the achieved several datasets in a common reference frame. The datasets can be taken from different viewpoints, at different times or by different sensors.^[17] In addition to the different dimensions of the datasets (2D and 3D) they have different scales, which are based on different contrasts and are collected at different times. Generally, registration methods can be subdivided in feature-based and intensity-based techniques,^[14] whereas first ones use edges, corners, lines, and curves and last ones use intensities or

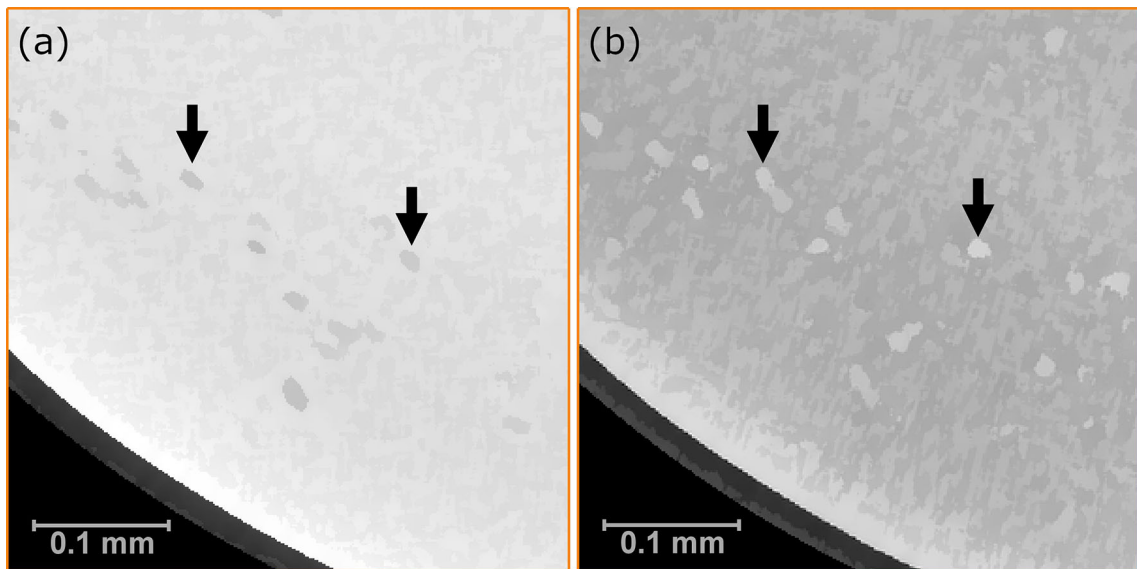


Fig. 12—Same parts of a virtual slice in the CT volumes generated from sample B before and after HIP rejuvenation showing the development of TCP phases at locations of initial pores, two locations are exemplarily indicated by arrows. (a) Slice from filtered CT volume of sample B before HIP rejuvenation showing internal pores in gray, alloy as bright area, and the surrounding air in dark gray and black. (b) Slice from the filtered CT volume of the HIP-rejuvenated sample B showing the alloy in gray, the surrounding air in dark gray and black, and the TCP phases appear as bright spots in the alloy at positions, where pores have been before the HIP rejuvenation.

gradients in small neighborhoods to find the correspondences.^[18] Because of the different modalities used for data collection, the intensity-based techniques were avoided and the focus was set to use features to find a suitable transformation. As features that are detected in both 2D and 3D datasets both the defects as well as the specimen surface are suitable for registration.

A defect in a SEM image is a two-dimensional object. Thus, the SEM image has to be compared to sections of the defect observed when virtually cutting the three-dimensional CT volume. The first image of Figure 11 shows exemplarily the outer surface of a complete pore as dark contour. The second image (Figure 11(b)) displays the section with the estimated layer position, whereas the two other images (Figures 11(c) and (d)) are generated by a section with a slightly tilted layer having only a small distance in between, wherein the outer surface of the pore is kept dark but the internal side of the pore is shown as light surface. Small changes of the plane orientation result in different pore shapes in the section planes. This effect makes it difficult to recognize an individual defect observed in a metallographic cross section in a corresponding virtual 3D volume from μ -CT.

In addition to the shape of single defects, the distances between defects in a section plane can be used to find the slice inside the virtual 3D volume which is matching to the metallographic 2D section. Or spoken in a more general way: the pattern of the defect distribution in a slice can be used to identify the position of this slice in the 3D volume. However, due to the difficulties to define the shape of a defect, as discussed above for a pore and

illustrated by Figure 11, it is also difficult to find in the 3D volume the mass centers of the defects observed as 2D objects in a metallographic section. An approximate measurement of distances between defects is nevertheless possible but elaborate, if the defect features have to be evaluated manually.

A third possibility to define features for a registration offers the surface of the specimen, which is represented in the SEM image as the border between the specimen and the embedding material. Such features are visible as white lines in Figure 9 at the right and left side of the visible slice.

In this study, the registration process using the features available in both 2D and 3D datasets was done manually. The yellow framed section in Figure 3 was particularly helpful, as it shows a very prominent defect on the sample surface. After registering the first slice, the next slices were looked for assuming that the planes of the metallographic cuts are parallel. By recognizing the features in the 2D planes of the several cuts in the CT volume, the correctness of the registration process is approved. However, the task of pattern recognition is certainly suitable for applying machine learning methods to create tools for automated registering.

B. Effect of HIP Rejuvenation on the Damages in the Fractured Fatigued Specimen

For evaluating the damage status of the LCF specimen before HIP rejuvenation, the data of the 3D CT volume from sample B, taken in the first μ -CT scan and the SEM micrographs of a metallographic

length section from sample A, were available. Multiple large pores and related defects are visible in both the 2D images of sample A in Figure 2 and the 3D representation of sample B in Figures 4(a) and (c), respectively. While in the SEM images cracks which are initiating at pores—especially at pores near the fracture site—can be distinguished, this is not always the case for the 3D representation, due to the limited resolution. Cracks initiating at the surface can be distinguished well in both SEM micrographs and CT volume because they are usually large.

Internal defects such as pores and cracks, the later mostly emanating from casting pores, were healed *via* HIP rejuvenation, which is visualized in the 3D CT representation in Figures 4(b) and (d), in the virtual slices of the CT volume in Figures 6(b), (d), and (f), and in the stitched SEM overview micrograph in Figure 8. In contrast, as expected, defects such as surface cracks or pores connected with the surface remained almost unchanged. By examining individual pores in the CT representation, examples were found, which appeared as internal pores isolated from the surface but proved to be connected to the surface since they appeared almost unaffected by the HIP rejuvenation. Some of the apparently internal defects, which effectively were connected to the surface, were found in the metallographic sections. They can be distinguished from internal isolated defects, since their surface is covered by oxides, compare Figure 10(c). According to the quantitative metallographic evaluation performed on the 2D cross section shown in Figure 8, the internal defects that have oxidation on the inner surface cover 0.07 area pct of the specimen, which is about a third of all internal defects measured in the considered section. Considering this observation and the total volumes of internal defects (Figure 5) before and after HIP rejuvenation treatment, a reduction of 87 vol pct of internal pores is estimated. This is less reduction than the reduction during HIP rejuvenation treatment of creep specimen estimated as 95 area pct,^[4] however, the LCF specimen was loaded until fracture.

Evaluating the CT volumes before and after HIP rejuvenation provides quantitative data about the change of defect fractions, the number and size of defects, and the volume fractions of internal defects and open cracks connected to the surface. The achieved database is statistically more representative than a dataset from evaluation of a single metallographic slice, as far as the same defect population is captured. For example, the defect fractions in virtual slices can differentiate regions inside or between dendrite cores when chosen a proper direction for slicing as shown in Figures 4, 6, and 7, and already discussed in Reference 10. Because small defects in the diameter range of a few voxel of the CT representation are detected reliably only by the high-resolution SEM analyses, a discrepancy can be obtained by quantifying internal defects from 2D and 3D characterization techniques. In this study, a slightly larger internal defect area was obtained using 2D SEM techniques, 0.19 area pct, compared to the area derived from the virtual corresponding section of the μ -CT, 0.17 area pct, which supports the comparison of data

between these two methods as well as shows that there was not a large number of tiny pores. Concerning the observation that the large individual defects in the sample volume seemed to be slightly decreased after HIP rejuvenation it is most likely an artefact occurring due to the post-processing of the μ -CT data.

However, in the case of cast materials with quite large pores, μ -CT evaluation captures the porosity which is relevant for the fatigue behavior. If smaller pores, *e.g.*, generated during thermal treatment, coexist with large solidification pores, their effect on crack initiation and growth can be neglected. Own unpublished investigations proved that in the case of CMSX-4 material manufactured by EPBF the typical pores evolving during solidification which are too small to be resolved reliably with the here used CT unit are not lifetime limiting. But larger defects do occur in pristine EPBF material and are preferred locations for the initiation of lifetime limiting cracks, even though they are quite rare as indicated by the scatter in fatigue life observed on specimens from the same EPBF material in LCF^[7,19] as well as in very high cycle fatigue (VHCF).^[20]

C. Consequences of the HIP Rejuvenation in the Fractured Fatigued Specimen

Another effect by HIP rejuvenation occurring at pores, even those not damaged by fatigue experience, is the formation of intermetallic precipitates, presumably TCP phases, at the sites of closed pores. This effect was observed and documented in Reference 10 by comparing SEM micrographs of cross sections and in Reference 7 by comparing fracture surfaces from specimens which were subjected to LCF in non-HIPed condition and from other specimens, which were LCF tested after HIP rejuvenation. However, since CT tomography is a non-destructive method, it allows for observing individual defects of the same specimen before and after HIP rejuvenation, and for the first time it has been shown for individual pore locations (dark spots in Figure 12(a)) that intermetallic phases occur at those locations after closure of the pores (bright spots in Figure 12(b)).

The SEM images of sample B after HIP rejuvenation display recrystallization of the entire specimen, see Figures 8 and 9(a), (c), and (d). Before HIP rejuvenation, the specimen was a single crystal. This is in line with the observations by SEM in electron backscatter (BSE) mode on metallographic sections of several CMSX-4 specimens, belonging to the same batch as the here investigated specimen, which have experienced LCF but no HIP rejuvenation and did not show recrystallization.^[10] Interestingly, samples from the same material, which have undergone high temperature creep and subsequent HIP rejuvenation with the same parameters as displayed in Figure 1, did not recrystallize.^[4] Presumably, in the performed LCF tests, localized stress concentrations at pores and crack tips are higher than in the mentioned creep tests, since the applied maximum stress in LCF was here 680 MPa while in the reported creep experiments^[4] the applied constant stress was 160 MPa. An indication for high localized stresses in the

LCF experiments is provided by the observation of massive plastic deformation at pores and crack tips, as can be recognized in Figures 2(a) and (b). Manifest indication for localized plastic deformations at cracks and pores such as traces of slip bands with deformed γ - γ' microstructure is also reported in literature for the same material, tested under the same LCF conditions until failure.^[10,21]

VI. SUMMARY AND CONCLUSIONS

In this study, a HIP procedure with integrated rejuvenation has been applied on samples made of cast CMSX-4 type material, denominated ERBO/1.^[8] The samples were taken from a specimen which has been subjected to LCF until fracture. The transformation of defects such as solidification pores and LCF cracks, mainly emanating from the pores, by means of the HIP rejuvenation procedure has been tracked in 3D by μ -CT before and after rejuvenation. Since the resolution of the μ -CT is limited by the voxel size (here 1.4 μ m) and small features such as pores, cracks, intermetallic TCP phases, and oxide scales on crack or pore surfaces, respectively, cannot be reliably discerned, SEM and μ -CT analyses were applied in a correlative approach. Results and benefits of this approach are as follows:

- The correlative approach has been proved successful in tracking microstructural changes caused by HIP rejuvenation on different length scales. Information on changes in damage statistics is achieved based on 3D μ -CT method, and details of damage characteristics are extracted from 2D SEM evaluation.
- With combined information on different length scales, defect populations isolated from the surface and such connected to the surface are distinguished.
- HIP rejuvenation is suitable to heal internal defects isolated from the surface. Defects with small connections with the surface can be recognized by comparing defect populations before and after HIP rejuvenation.
- Since μ -CT is a non-destructive method, the evolution of microstructural features can be traced on one identical sample.
- The formation of intermetallic precipitates at locations of pores during HIP rejuvenation has been shown the first time for individual pores/precipitates.
- In this study, registering of 2D and 3D features was performed mainly manually. Because of the benefits from applying the correlative approach and because the task of pattern recognition is certainly suitable for applying machine learning methods, it is worth the effort to create tools for automated registering.
- SEM imaging revealed complete recrystallization of the LCF sample, which was not observed in the case of HIP rejuvenated creep specimens. After LCF, localized high plastic deformation occurs at defects and enhances presumably the recrystallization. Since

the fractured LCF sample was extremely deformed, it is worth to repeat the HIP rejuvenation experiment on samples with a damage status close to what is realistic in technical applications.

- With the experience of this work, it would be interesting to track the microstructural changes from pristine material to samples which have been subjected to LCF.

ACKNOWLEDGMENTS

The authors acknowledge funding by the Deutsche Forschungsgemeinschaft (DFG) in the framework of the collaborative research center SFB/TR 103 on single crystal superalloys through the projects A3 (AD, MB) and T4 (ILG, BT, WT). The authors further acknowledge the center for interface-dominated high-performance materials (Zentrum für Grenzflächendominierte Höchstleistungswerkstoffe, ZGH) at the Ruhr University Bochum for the use of the computed tomography scanner and the support from Dr. Johannes Boes.

CONFLICT OF INTEREST

The authors declared that they have no conflict of interest.

OPEN ACCESS

This article is licensed under a Creative Commons Attribution 4.0 International License, which permits use, sharing, adaptation, distribution and reproduction in any medium or format, as long as you give appropriate credit to the original author(s) and the source, provide a link to the Creative Commons licence, and indicate if changes were made. The images or other third party material in this article are included in the article's Creative Commons licence, unless indicated otherwise in a credit line to the material. If material is not included in the article's Creative Commons licence and your intended use is not permitted by statutory regulation or exceeds the permitted use, you will need to obtain permission directly from the copyright holder. To view a copy of this licence, visit <http://creativecommons.org/licenses/by/4.0/>.

REFERENCES

1. R.C. Reed: *The Superalloys: Fundamentals and Applications*, Cambridge University Press, Cambridge, 2006.
2. J.-Y. Guédou and L. Rémy: in *Nickel Base Single Crystals Across Length Scales*, G. Cailletaud, J. Cormier, G. Eggeler, V. Maurel, and L. Nazé, eds., Elsevier, Amsterdam, 2022, pp. 3–19.

3. A.I. Epishin, T. Link, B. Fedelich, I.L. Svetlov, and E.R. Golubovskiy: *Matec Web Conference*, vol. 14, 2014. <https://doi.org/10.1051/mateconf/20141408003>.
4. B. Rutttert, D. Bürger, L.M. Roncery, A.B. Parsa, P. Wollgramm, G. Eggeler, and W. Theisen: *Mater. Des.*, 2017, vol. 134, pp. 418–25. <https://doi.org/10.1016/j.matdes.2017.08.059>.
5. B. Rutttert, O. Horst, I. Lopez-Galilea, D. Langenkamper, A. Kostka, C. Somsen, J.V. Goerler, M.A. Ali, O. Shchyglo, I. Steinbach, G. Eggeler, and W. Theisen: *Metall. Mater. Trans. A*, 2018, vol. 49A, pp. 4262–73. <https://doi.org/10.1007/s11661-018-4745-6>.
6. O.M. Horst, B. Rutttert, D. Bürger, L. Heep, H. Wang, A. Dlouhy, W. Theisen, and G. Eggeler: *Mater. Sci. Eng. A Struct.*, 2019, vol. 758, pp. 202–14. <https://doi.org/10.1016/j.msea.2019.04.078>.
7. C. Meid, A. Dennstedt, M. Ramsperger, J. Pistor, B. Rutttert, I. Lopez-Galilea, W. Theisen, C. Körner, and M. Bartsch: *Scripta Mater.*, 2019, vol. 168, pp. 124–28. <https://doi.org/10.1016/j.scriptamat.2019.05.002>.
8. A.B. Parsa, P. Wollgramm, H. Buck, C. Somsen, A. Kostka, I. Povstugar, P.P. Choi, D. Raabe, A. Dlouhy, J. Müller, E. Spiecker, K. Demtroder, J. Schreuer, K. Neuking, and G. Eggeler: *Adv. Eng. Mater.*, 2015, vol. 17, pp. 216–30. <https://doi.org/10.1002/adem.201400136>.
9. C. Meid, U. Waedt, A. Subramaniam, J. Wischek, M. Bartsch, P. Terberger, and R. Vassen: *Materialwiss Werkst.*, 2019, vol. 50, pp. 777–87. <https://doi.org/10.1002/mawe.201800135>.
10. C. Meid: Ruhr-Universität Bochum, Universitätsbibliothek, 2019. <https://doi.org/10.13154/294-6347>.
11. “AVIZO”: <http://www.thermofisher.com/amira-avizo>. Accessed 04 August 2022.
12. D. Baum and J. Titschack: *EuroVis 2016—Short Papers*, 2016, pp. 113–17. <https://doi.org/10.2312/eurovisshort.20161171>.
13. L.G. Brown: *Comput. Surv.*, 1992, vol. 24, pp. 325–76. <https://doi.org/10.1145/146370.146374>.
14. A.R. Durmaz, N. Hadzic, T. Straub, C. Eberl, and P. Gumbsch: *Exp. Mech.*, 2021, vol. 61, pp. 1489–1502. <https://doi.org/10.1007/s11340-021-00758-x>.
15. “Image Composite Editor”: <https://www.microsoft.com/en-us/research/project/image-composite-editor/>. Accessed 04 August 2022.
16. C. Meid: Images Prepared in Frame of PhD work, provided as courtesy by the author of the thesis.
17. E. Saiti and T. Theoharis: *Comput. Graph.*, 2020, vol. 91, pp. 153–78. <https://doi.org/10.1016/j.cag.2020.07.012>.
18. A. Goshtasby: *2-D and 3-D Image Registration: for Medical, Remote Sensing, and Industrial Applications*, Wiley, Incorporated, 2005.
19. C. Körner, M. Ramsperger, C. Meid, D. Bürger, P. Wollgramm, M. Bartsch, and G. Eggeler: *Metall. Mater. Trans. A*, 2018, vol. 49A, pp. 3781–92. <https://doi.org/10.1007/s11661-018-4762-5>.
20. L.M. Bortoluci Ormastroni, I. Lopez-Galilea, J. Pistor, B. Rutttert, C. Körner, W. Theisen, P. Villechaise, F. Pedraza, and J. Cormier: *Addit. Manuf.*, 2022. <https://doi.org/10.1016/j.addma.2022.102759>.
21. C. Meid, M. Eggeler, P. Watermeyer, A. Kostka, T. Hammer-schmidt, R. Drautz, G. Eggeler, and M. Bartsch: *Acta Mater.*, 2019, vol. 168, pp. 343–52. <https://doi.org/10.1016/j.actamat.2019.02.022>.

Publisher’s Note Springer Nature remains neutral with regard to jurisdictional claims in published maps and institutional affiliations.